



ALMA CO Clouds and Young Star Complexes in the Interacting Galaxies IC 2163 and NGC 2207

Debra Meloy Elmegreen¹, Bruce G. Elmegreen², Michele Kaufman³, Elias Brinks⁴, Curtis Struck⁵, Frédéric Bournaud⁶, Kartik Sheth⁷, and Stephanie Juneau⁶

¹ Department of Physics & Astronomy, Vassar College, Poughkeepsie, NY 12604, USA; elmegreen@vassar.edu

² IBM Research Division, T.J. Watson Research Center, P.O. Box 218, Yorktown Heights, NY 10598, USA; bge@us.ibm.com

³ 110 Westchester Road, Newton, MA 02458, USA; kaufmanrallis@icloud.com

⁴ University of Hertfordshire, Centre for Astrophysics Research, College Lane, Hatfield AL10 9AB, UK; e.brinks@herts.ac.uk

⁵ Department of Physics & Astronomy, Iowa State University, Ames, IA 50011, USA; struck@iastate.edu

⁶ Laboratoire AIM-Paris-Saclay, CEA/DSM-CNRS-Université Paris Diderot, Irfu/Service d'Astrophysique, CEA Saclay, Orme des Merisiers, F-91191 Gif sur Yvette, France; frederic.bournaud@gmail.com, stephanie.juneau@cea.fr

⁷ NASA Headquarters, Washington, DC 20546, USA

Received 2016 October 4; revised 2017 March 28; accepted 2017 April 3; published 2017 May 22

Abstract

Atacama Large Millimeter Array (ALMA) observations of CO(1-0) emission in the interacting galaxies IC 2163 and NGC 2207 are used to determine the properties of molecular clouds and their association with star-forming regions observed with the *Hubble Space Telescope*. Half of the CO mass is in 249 clouds, each more massive than $4.0 \times 10^5 M_{\odot}$. The mass distribution functions for the CO clouds and star complexes in a galactic-scale shock front in IC 2163 both have a slope on a log–log plot of -0.7 , similar to what is observed in Milky Way clouds. The molecular cloud mass function is steeper in NGC 2207. The CO distribution in NGC 2207 also includes a nuclear ring, a mini-bar, and a mini-starburst region that dominates the $24 \mu\text{m}$, radio, and $\text{H}\alpha$ emission in both galaxies. The ratio of the sum of the masses of star complexes younger than 30 Myr to the associated molecular cloud masses is $\sim 4\%$. The maximum age of star complexes in the galactic-scale shock front in IC 2163 is about 200 Myr, the same as the interaction time of the two galaxies, suggesting the destruction of older complexes in the eyelids.

Key words: galaxies: individual (IC 2163, NGC 2207) – galaxies: interactions – galaxies: ISM – galaxies: spiral – galaxies: star clusters: general

1. Introduction

The spiral galaxies IC 2163 and NGC 2207 are a well-studied pair undergoing a grazing collision, previously observed in the X-ray, UV, optical, infrared, millimeter, and centimeter wavelengths (Elmegreen et al. 1995a, 1995b, 2000, 2001, 2006, 2016; Kaufman et al. 2012) and modeled in simulations (Elmegreen et al. 1995b; Struck et al. 2005). The close encounter produced in-plane tidal forces in IC 2163, resulting in a large shock producing a cuspy-oval, or “eyelid,” structure at mid-radius, and long tidal arms. The encounter also produced forces nearly orthogonal to the plane of NGC 2207, resulting in a warp. Details of the interaction are given in the cited papers.

Atacama Large Millimeter Array (ALMA) observations of ^{12}CO (1-0) were presented in two recent papers. Paper I (Elmegreen et al. 2016) studied the Kennicutt–Schmidt (Kennicutt & Evans 2012) relation for star formation and suggested that some regions in NGC 2207 with high star formation rates ($>10^{-2} M_{\odot} \text{pc}^{-2} \text{Myr}^{-1}$) have a fraction of molecular to total gas of less than 0.5 as a result of unusually high turbulent speeds. Paper II (Kaufman et al. 2016) showed $\sim 100 \text{ km s}^{-1}$ streaming motions in the eyelids that trace the pile-up of molecular gas. Here, in Section 2 we investigate the individual molecular clouds seen with ALMA and measure their associated star complexes and OB associations. Section 3


discusses Feature *i* and the nuclear region of NGC 2207. Our conclusions are in Section 4.

2. Observations and Analysis of CO Clouds

2.1. Data

IC 2163 and NGC 2207 are at a distance of 35 Mpc (NASA/IPAC Extragalactic Database, NED). As described in Papers I and II, ALMA observations of the 2.6 mm line from the ^{12}CO (1-0) transition were made in 34 pointings, with a point-spread function of $2''.00 \times 1''.52$ (HPBW), a channel width of 10 km s^{-1} , and an rms noise per channel of $3.7 \text{ mJy beam}^{-1}$. Further data reduction techniques are given in Papers I and II. The *Hubble Space Telescope* (HST) WFPC2 data used in this paper are from our observations (Elmegreen et al. 2000, 2001) taken with filters F336W (U), F439W (B), F555W (V), and F814W (I). The IR data are from *Spitzer* IRAC observations at $8 \mu\text{m}$ and MIPS observations at $24 \mu\text{m}$ (Elmegreen et al. 2006). Radio continuum observations at 6 cm observed with the Karl G. Jansky Very Large Array⁸ are described in Kaufman et al. (2012).

Figure 1 shows a composite color image with F336W in blue, IRAC channel 4 ($8 \mu\text{m}$) in green, and CO in red. (Figure 1 in Paper II showed the CO emission overlaid on the F439W image.) The strongest CO emission is found in the eyelids of IC 2163 and “Feature *i*” (Section 3.1) in the northwest tip of NGC 2207; these features are bright in all passbands, as is the nuclear

 Original content from this work may be used under the terms of the [Creative Commons Attribution 3.0 licence](https://creativecommons.org/licenses/by/3.0/). Any further distribution of this work must maintain attribution to the author(s) and the title of the work, journal citation and DOI.

⁸ The National Radio Astronomy Observatory is a facility of the National Science Foundation operated under cooperative agreement by Associated Universities, Inc.

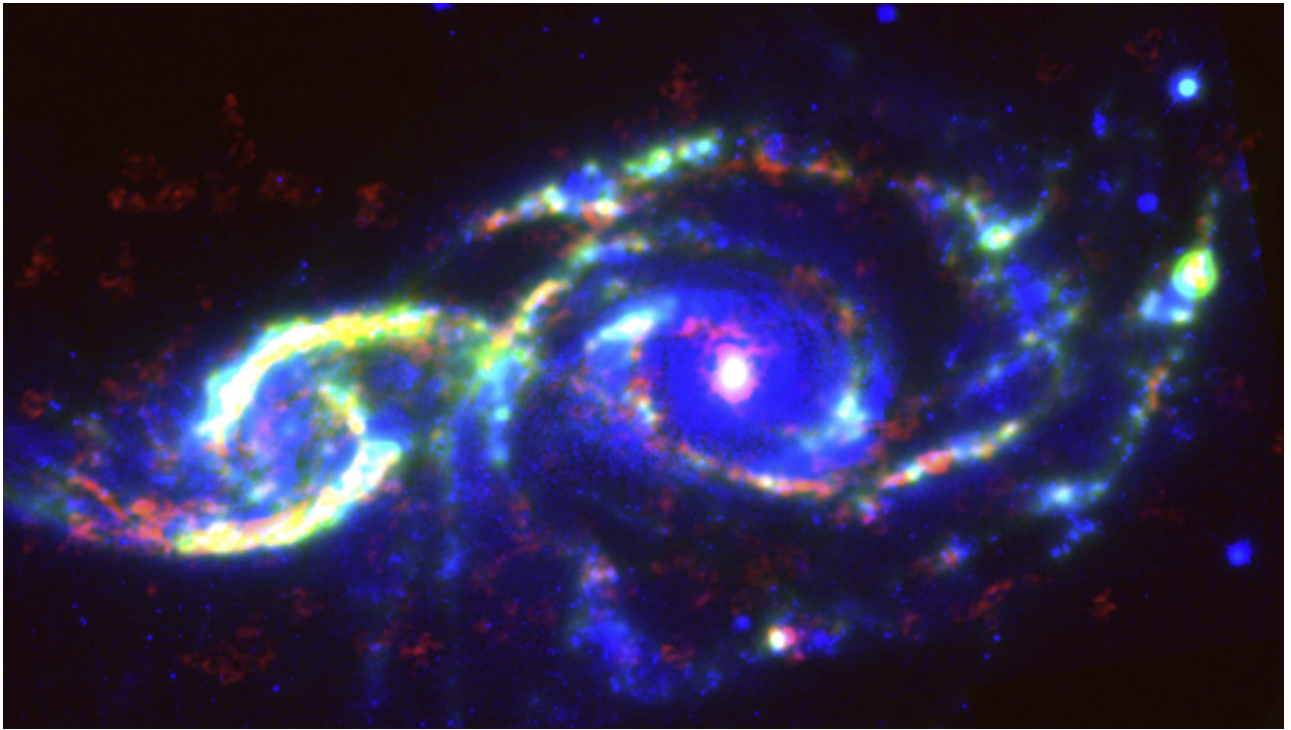


Figure 1. Color composite showing *HST* WFPC2 F336W in blue, *Spitzer* IRAC channel 4 ($8\ \mu\text{m}$) in green, and ALMA ^{12}CO (1-0) in red. North is up. The “eyelids” of IC 2163 are the bright yellow arms to the east (left). Feature *i* in NGC 2207 is the bright yellow circular region in the tip of the western (right) arm of NGC 2207.

region of NGC 2207. CO emission also appears in smaller clouds throughout the galaxies, most prominently in the arms.

2.2. Identification of CO Clouds

Paper I determined the total molecular mass detected by our interferometric observations. For IC 2163, the H_2 mass is $2.1 \times 10^9 M_\odot$ and for NGC 2207, it is $2.3 \times 10^9 M_\odot$. Here, we focus on individual CO clouds, identified using several steps involving either intensity or velocity data. After creating a blanking mask via the technique of smooth-plus-velocity continuity (cf. Papers I and II) and applying it to the original unsmoothed cube, we identified 327 discrete CO clouds by eye in the resulting surface density image in DS9. To be conservative in setting a limit for discriminating between clouds and noise spikes, we then considered in the following analysis only clouds that contained 2 or more pixels ($2\ \text{px} = 1''.0 = 170\ \text{pc}$ at the assumed distance of 35 Mpc) above a CO intensity $I(\text{CO}) = 200\ \text{Jy beam}^{-1} \text{m s}^{-1}$, which corresponds to a line of sight (LOS) column density $N(\text{H}_2)$ of $17.7 M_\odot \text{pc}^{-2}$. Many of the small clouds north and south of the eyelids of IC 2163 and in the interarm regions of NGC 2207 are below the selected contour limit. There are 26 such faint clouds, and they amount to 1.3% of the summed cloud mass. Without these clouds, there were 301 clouds remaining in the sample.

Next, we eliminated clouds that had at most one velocity channel above 2σ , where σ is the rms noise ($=3.7\ \text{mJy beam}^{-1} = 0.11\ \text{K}$) in the unsmoothed cube, and we eliminated additional clouds that were smaller than our spatial resolution of $2''.0 \times 1''.5$. The final number of clouds was then 249; these are used in the following analysis. They are the dense, large-scale, CO-emitting regions that stand out amidst the more diffuse CO emission in the galaxies. Such regions are

sometimes referred to as Giant Molecular Associations (GMAs), but here we call them clouds.

Figure 2 is a color-coded display of the CO emission, where the color represents the number of channels brighter than a given noise level. The black pixels in the figure are for positions with 0 or 1 velocity channels brighter than 2σ , blue pixels are for 2 channels brighter than 2σ , yellow pixels are for 3 channels brighter than 2σ , and pixels are for 4 or more channels brighter than 2σ . All of the clouds discussed in this paper are in these colored regions.

In a separate search for clouds, we also ran the CO intensity image through the source extraction program SExtractor (Bertin & Arnouts 1996). The parameter DETECT_MINAREA, which is the minimum number of pixels above threshold, was set to 20; the analysis threshold, ANALYSIS_THRESH, was set to $10\sigma_{\text{SEX}}$ for rms σ_{SEX} defined by SExtractor, and the deblending threshold, DEBLEND_THRESH, was set to 32. This procedure yielded 178 CO clouds. With these parameters, SExtractor detected the well-separated CO clouds that we identified by eye, but the segmentation maps from SExtractor put all of the CO in the eyelids of IC 2163 into a single cloud even though discrete CO clouds can be seen clearly. SExtractor also put all of the CO in the southern inner main arm of NGC 2207 into a single cloud. Separation of these bright regions into clouds required different thresholds. In what follows we use the visual identifications of clouds.

2.3. CO Masses

Photometry on the visually identified CO clouds was done with the Image Reduction and Analysis Facility (IRAF) task *imstat*, in which a variable rectangle is drawn around each cloud in order to match the cloud size based on isophotal limits; this task then determines a total intensity based on the average intensity times the number of pixels. This method is analogous

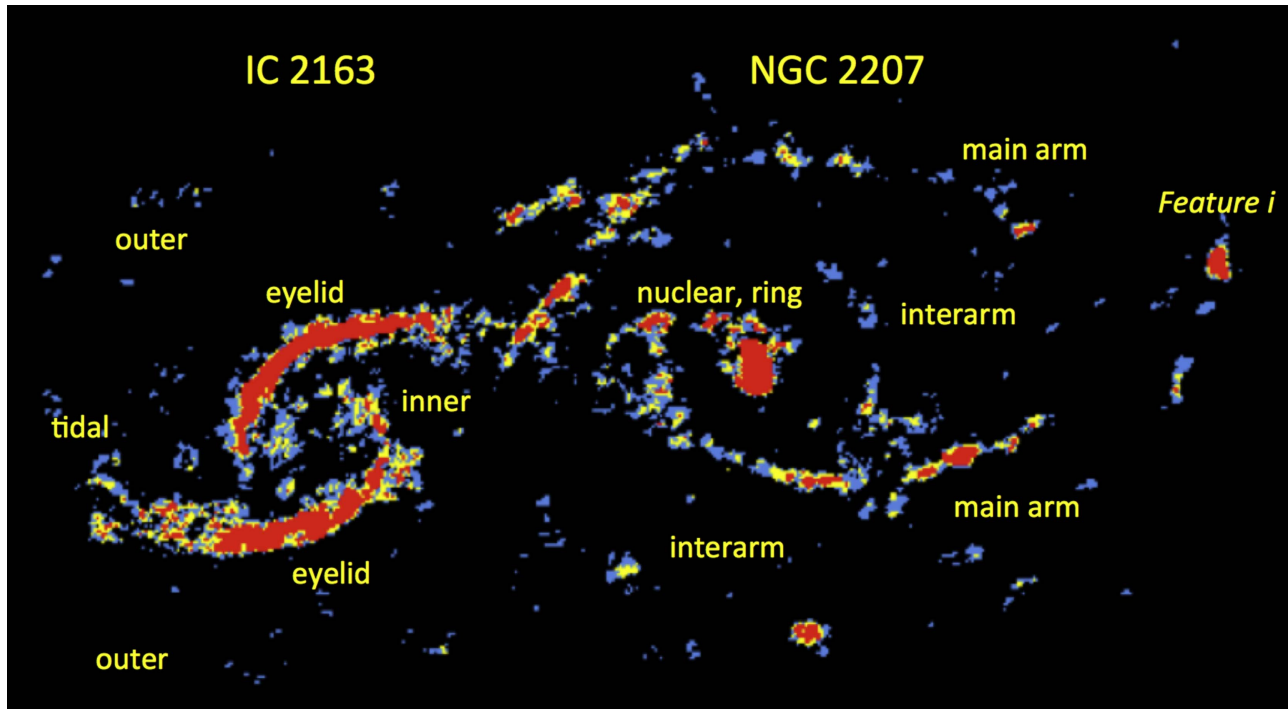


Figure 2. This is a color-coded display of the CO emission, where the color represents the number of channels brighter than some noise level. The black pixels in the figure are for positions with 0 or 1 velocity channels brighter than 2σ , blue pixels are for 2 channels brighter than 2σ , yellow pixels are for 3 channels brighter than 2σ , and pixels are for 4 or more channels brighter than 2σ .

to aperture photometry using a variable aperture, but is useful for outlining elongated cloud regions with rectangles instead of circles. The background was not subtracted because the background was already blanked in this image as a result of applying a mask to the CO cube. To convert the CO emission into molecular mass $M(\text{H}_2)$, we use $X_{\text{CO}} = 1.8 \pm 0.3 \times 10^{20} \text{ H}_2 \text{ cm}^{-2} (\text{K km s}^{-1})^{-1}$ from Dame et al. (2001). All cloud masses given in this paper are H_2 masses and should be multiplied by 1.36 to get the total gas mass, including helium and heavy elements. The sum of the cloud H_2 masses is $7.4 \times 10^8 M_\odot$ for IC 2163 and $9.1 \times 10^8 M_\odot$ for NGC 2207. These are 35% and 40%, respectively, of the total H_2 masses measured in Paper I.

At the ALMA resolution of $2''.00 \times 1''.52$, which is $340 \times 260 \text{ pc}$, anything detected here as a CO cloud is a large region of molecular material; $10^6 M_\odot$ spread out over the beam size corresponds to an average surface density of $11 M_\odot \text{ pc}^{-2}$, which is only about one-tenth the surface density of a typical Milky Way CO cloud.

For comparison purposes, the clouds are divided into six large regions. Three regions are in IC 2163: (a) the eyelids, (b) the inner arms plus the tidal arms, and (c) the outer regions beyond the arms. In NGC 2207, the three regions are (a) the main spiral arms, (b) the nuclear region plus nuclear ring, and (c) the interarm regions. Figure 3 shows histograms of the logs of the cloud masses for the six regions, binned in $\log_{10}(M/M_\odot)$ units of 0.2. For reference, a red line with $\log_{10}(M/M_\odot) = 6.5$ is shown in each plot; this is the average value for the inner and tidal arms of IC 2163 and the main arms of NGC 2207. The minimum detected cloud mass was $\log_{10}(M/M_\odot) = 5.6$. The most massive cloud in either galaxy is in the nuclear region of NGC 2207, with $\log_{10}(M/M_\odot) = 8.0$. The eyelid regions of IC 2163 contain clouds with the highest average, with $\log_{10}(M/M_\odot) = 7.2$; all have $\log_{10}(M/M_\odot)$ greater than 6.6,

and 12 have $\log_{10}(M/M_\odot) = 7$ or greater. The tidal arms of IC 2163 have cloud masses similar to those in the main arms of NGC 2207, and the clouds in the outer, non-arm regions of both galaxies are less massive and also similar to each other in mass.

It is interesting to compare these masses with high-resolution studies of other interacting galaxies. Koda et al. (2009) observed CO in M51 using CARMA and NRO with an angular resolution corresponding to 160 pc. In their Figure 2, they showed the distribution of giant molecular clouds (GMCs), which they define as having $\log_{10}(M/M_\odot)$ of 5–6, and of GMAs, with log masses of 7–8. The GMAs are located exclusively in the spiral arms of M51, as they are in the eyelid regions of IC 2163 (and a few in the main arms of NGC 2207) in this study. Their GMCs are also mostly in the M51 arms, but there are many in the interarm regions, similar to the distribution of lower-mass clouds in IC 2163 and NGC 2207. They concluded that GMAs have lifetimes of a few tens of millions of years, associated with the arm crossing times. Wei et al. (2012) used the Submillimeter Array and the Plateau de Bure Interferometer to observe CO(2-1) with an angular resolution of 160 pc in the Antennae colliding galaxies, NGC 4038 and NGC 4039. They found $\log_{10}(M/M_\odot)$ ranging from 5 to 8, with the most massive clouds in the regions of the most intense star formation.

The combined cloud mass function is shown in the left panel of Figure 4, binned in $\log_{10}(M/M_\odot)$ intervals of 0.2. Clouds in the eyelids are shown as red dots, while all others are shown as black circles. The linear fitting functions for each sample are shown in the matching color. The eyelid cloud mass function has a slope of -0.7 ± 0.1 , while the rest of the clouds have a slope of -1.3 ± 0.1 . For only the clouds in the main arms of NGC 2207, shown in the upper right panel of Figure 3, the slope is -1.6 ± 0.1 . For reference, the mass function for

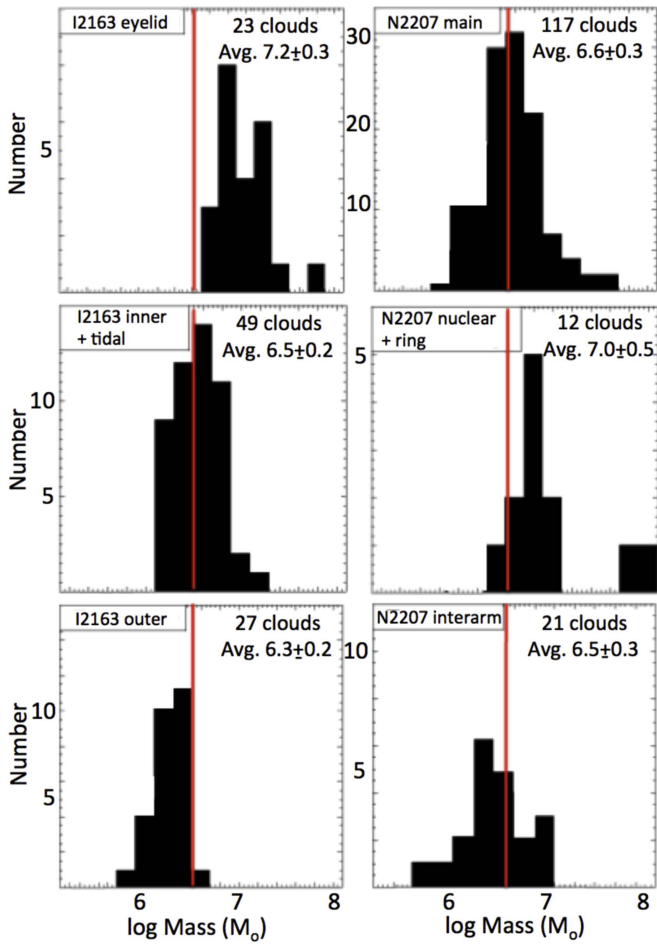


Figure 3. Histogram of the logs of the cloud masses for different regions of IC 2163 (eyelids, inner plus tidal arms, outer regions) and NGC 2207 (main arms, inner ring, inter arms). The red line is a fiducial marker for $\log_{10}(M/M_{\odot}) = 6.5$, which is the average for the inner plus tidal arm clouds of IC 2163 and the interarm clouds of NGC 2207. The number of clouds and their average masses in the logarithm are indicated for each region.

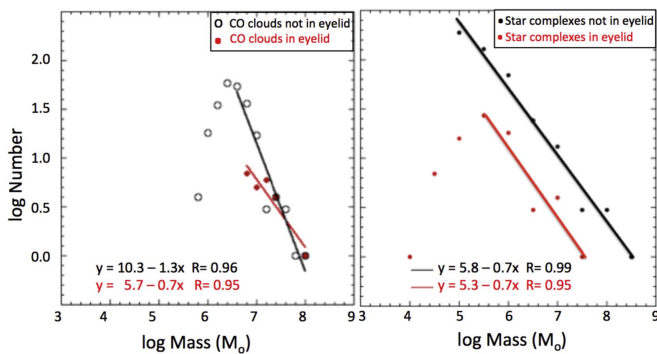


Figure 4. (Left) $\log(\text{Number})$ vs. $\log_{10}(M/M_{\odot})$ for all clouds in both IC 2163 and NGC 2207, binned in $\log_{10}(M/M_{\odot})$ intervals of 0.2. The red dots are clouds in the eyelids of IC 2163 only; the black dots are the rest of the clouds in both galaxies. The power-law slope is -0.7 ± 0.1 for the eyelid clouds and -1.3 ± 0.1 for the rest of the clouds. (Right) $\log(\text{Number})$ vs. $\log_{10}(M/M_{\odot})$ for star complexes (black dots) in both galaxies except for the eyelids, and only in the eyelids (red dots), binned in $\log_{10}(M/M_{\odot})$ intervals of 0.5. The power-law slope is the same for both, -0.7 ± 0.1 .

clouds identified by SExtractor has the same slope in the $\log_{10}(M/M_{\odot})$ range of 6.6 to 7.6 (-1.3 with a goodness of fit $R = 0.99$) as the mass function for the visually identified clouds in Figure 4.

The large slopes outside of the eyelid region are steep compared to the mass function of inner Milky Way molecular clouds, where the power-law slope for equal intervals of $\log_{10}(M/M_{\odot})$ is between -0.4 and -0.6 (Rosolowsky 2005); they are more comparable to those estimated for the outer Milky Way, which range between -1 and -1.6 (Rosolowsky 2005). In M33, the slope was measured to be -1.85 by Rosolowsky (2005), -1.1 between 2 and 4 kpc by Rosolowsky et al. (2007), and to steepen from -0.6 ± 0.2 in the inner 2 kpc to -1.3 ± 0.2 beyond 2 kpc by Gratier et al. (2012). In the Antennae, Wei et al. (2012) derived an equally steep power-law slope of ~ -1.4 up to $10^{6.5} M_{\odot}$. In M51, however, the slopes are more like they are in the Milky Way: Colombo et al. (2014) measured CO (1-0) cloud masses at 40 pc resolution and derived mass spectrum slopes ($\gamma + 1$ in their notation) of -0.6 to -0.8 up to $10^7 M_{\odot}$ in the ring and density wave arms. They did find, however, the slope steepness for higher-mass clouds. Some of these differences may reflect different cloud identification methods. Miville-Deschênes et al. (2017), for example, got a slope of -3.0 ± 0.1 for equal intervals of $\log M$ at the high-mass end of Milky Way CO clouds.

2.4. Mass Spectrum Variations

The reason for these variations in the CO cloud mass spectrum slope are unknown. The power spectrum of cloud structure seems to be a nearly universal power law for a range of scales up to the thickness of a galaxy (Stanimirovic et al. 1999, 2000; Elmegreen et al. 2001; Block et al. 2010; Combes et al. 2012; Zhang et al. 2012). The mass function for clouds should follow from the power spectrum slope of cloud structure (Shadmehri & Elmegreen 2011). But this is the mass spectrum for total cloud structure and not just the mass of the CO-emitting part. If the fraction of cloud mass in the form of CO decreases with increasing cloud mass, then the CO cloud mass spectrum will be steeper than the total cloud mass spectrum. For example, Paper I suggested that some star-forming regions with high SFRs in NGC 2207 are H I-dominated with relatively small CO cores. The largest clouds in the non-eyelid regions would then have a lower molecular fraction than the clouds in the eyelids. This could cause the molecular mass spectrum to drop more quickly than the total cloud mass spectrum in the non-eyelid regions.

A specific example where the molecular mass fraction per cloud decreases with increasing cloud mass is if the cloud edge always has a density too low for CO formation or excitation, and the density gradient inside the cloud gets steeper with increasing total mass. Then the CO core of the cloud would shrink relative to the whole cloud as the total mass increased. This changing density gradient is reasonable because the virial parameter α decreases with increasing mass in most CO surveys (e.g., Miville-Deschênes et al. 2017), and a lower virial parameter corresponds to stronger self-gravity and a more concentrated cloud core.

To quantify this model, consider that the mass of the CO part of a cloud, M_{CO} (which in the previous section we converted to $M(\text{H}_2)$) increases with the total cloud mass, M_{tot} , as $M_{\text{CO}} \propto M_{\text{tot}}^{\zeta}$ for $\zeta < 1$. Suppose also that the total mass spectrum of interstellar structure is $dN(M_{\text{tot}})/dM_{\text{tot}} \propto M_{\text{tot}}^{-\beta}$. Then the mass spectrum of the CO parts of the clouds may be derived from the one-to-one relation between the two, $N(M_{\text{CO}})dM_{\text{CO}} = N(M_{\text{tot}})dM_{\text{tot}}$, from which we obtain $dN(M_{\text{CO}})/dM_{\text{CO}} \propto M_{\text{CO}}^p$ for $p = -(\beta + \zeta - 1)/\zeta$. If β is in

the likely range from 1.5 to 2, then p is more negative than β . That means that the mass spectrum of CO-identified “clouds” is steeper than the mass spectrum of the physical cloud structure. The slope of $p \sim -2.3$ for CO clouds derived above (-1.3 for equal intervals of $\log M$) requires $\zeta \sim 0.4$ to 0.8 for these β , respectively.

Another consideration is that for typical interstellar clouds, there is an inverse relation between average cloud density and mass (Larson 1981). If there is a corresponding decrease in molecular fraction at lower average cloud density, then this CO mass fraction decreases with increasing total mass. For example, Miville-Deschênes et al. (2017) derived a fractal mass–radius relation $M_{\text{CO}} = 36.7R_{\text{CO}}^{2.2}$ for CO cloud radius R_{CO} in pc. This fractal power is also about the same as that determined by other studies, even for atomic and dust masses (Sánchez et al. 2005). The Miville-Deschênes et al. (2017) relation gives an average H_2 molecular density for the CO part of the cloud $n = 620R^{-0.8} \text{ cm}^{-3}$, which is $n = 2300M_{\text{CO}}^{-0.36} \text{ cm}^{-3}$ (assuming a mean molecular weight of $4 \times 10^{-24} \text{ g}$). Observations that trace only molecules in an interstellar medium that is partially molecular should show a rapid drop in the molecular cloud mass function as the average cloud density drops and the clouds turn atomic at higher masses. This explanation would apply to the outer regions of the galaxies mentioned above where the steep mass function slopes were observed. It would not apply to the inner part of the Milky Way or M51 or the IC 2163 eyelids, where the slope is shallower, because the clouds in these regions are highly molecular.

2.5. Star-forming Complexes and CO Clouds

In order to compare the locations and masses of the optical star-forming regions with the locations and masses of the CO clouds, we ran SExtractor on the F439W images for each galaxy to identify the most prominent star-forming regions. These positions were then used to extract the corresponding sources in the F336W, F555W, and F814W images. Foreground stars were removed using the task *imexamine* to eliminate point sources with Gaussian profiles. There are 733 identified star-forming regions. One pixel in the *HST* images is $0''.1$, which corresponds to 16.9 pc. The selected star-forming regions were restricted to 10 contiguous pixels greater than the 10σ threshold, so the lower limit to the sizes of the regions is about 50 pc. Population synthesis fits to determine ages and masses based on the photometric magnitudes and colors for solar abundance were performed using the methods described in Elmegreen et al. (2012), with models from Bruzual & Charlot (2003) including extinction from Calzetti et al. (2000) and Leitherer et al. (2002). The star formation history for each region was assumed to be a decaying exponential with a decay time of 10 Myr.

The mass distribution function for the star complexes is shown in Figure 4 (right), with $\log(\text{Number})$ versus $\log_{10}(M/M_{\odot})$ for the eyelid region complexes (red dots) and the rest of the complexes (black dots), binned in log-mass intervals of 0.5. The fits to the high-mass end are indicated by red and black lines, respectively. The slopes are the same, -0.7 ± 0.1 , even though the star formation activity differs in these two types of regions. This slope is also the same as that for the mass distribution function of the CO clouds in the eyelids (Figure 4, left).

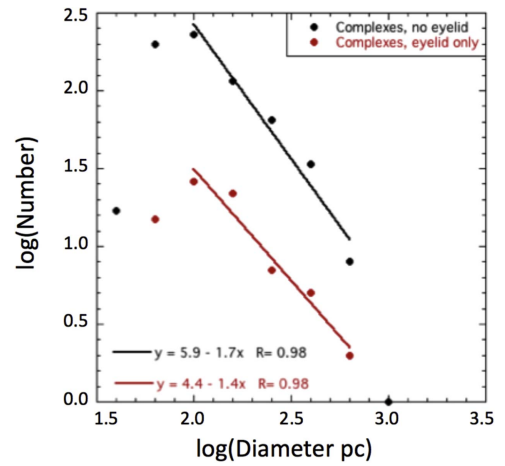


Figure 5. Distribution of $\log(\text{Number})$ vs. $\log(\text{Diameter})$ of SExtractor-fitted star-forming complexes for the eyelid region (red) and the other regions combined (black). Size is determined from the square root of the number of *HST* pixels. The slopes from $\log(\text{Diameter}) = 2.0$ – 2.8 are indicated for the two samples. The distributions turn over at the low size end, and there is only one complex at $\log(3.0)$.

For the Antennae galaxies, Wei et al. (2012) compared the cloud mass function with the super star cluster mass function, and concluded that the slopes are similar to each other (-1.4 and -2 , respectively). Thus, in the Antennae and in IC 2163 and NGC 2207, slopes for mass functions in star-forming regions are similar to the clouds in which they formed.

The size distributions of the SExtractor-fitted sources are shown in Figure 5, binned in $\log(\text{Diameter})$ intervals of 0.5. Most fitted sources have a diameter of about 100 pc, which means they are several pixels square in the images. These are not star clusters, which would have a size of ~ 5 pc or less, but OB associations or giant star complexes (Efremov 1995). Unlike star complexes of this size in the Milky Way, which tend to be ~ 30 – 50 Myr old, some of the regions with the same size in IC 2163 and NGC 2207 are very young, with an age of ~ 1 Myr. Nevertheless, we refer to them as star complexes in what follows. The size distribution in the eyelids has a slope of -1.4 , compared with a slope of -1.7 in the other regions of the galaxies, in the $\log(\text{Diameter})$ range of 2.0 to 2.8. The distributions turn over at the low size end from incompleteness; there is only 1 complex in the 1 kpc size bin.

Figure 6 (Left) shows a log–log plot of star complex photometric mass as a function of photometric age for all complexes except those in the eyelids (top) and for only those in the eyelids (bottom). The models are not accurate for ages below 3×10^6 years, so these complexes will be ignored. There is the usual trend of increasing mass with age. The lower-mass limit for this trend is because of star complex fading with time. The upper-mass limit is the size-of-sample effect, where the mass of the most massive complex increases with the number of complexes, and the number of complexes per unit log time increases with time when the formation rate is constant (Hunter et al. 2003; Elmegreen & Hunter 2010).

Figure 6 suggests there may be a cutoff in age for eyelid complexes compared with the rest of the complexes. To determine whether this cutoff is statistically significant, we consider the number of regions in various age intervals. Only 1 out of the 77 star complexes in the eyelids is older than 2×10^8 year, compared with 34 out of 656 that are at least this age in the other parts of the galaxies.

The difference in complex ages for the eyelids compared with elsewhere is shown on the right side of Figure 6, where

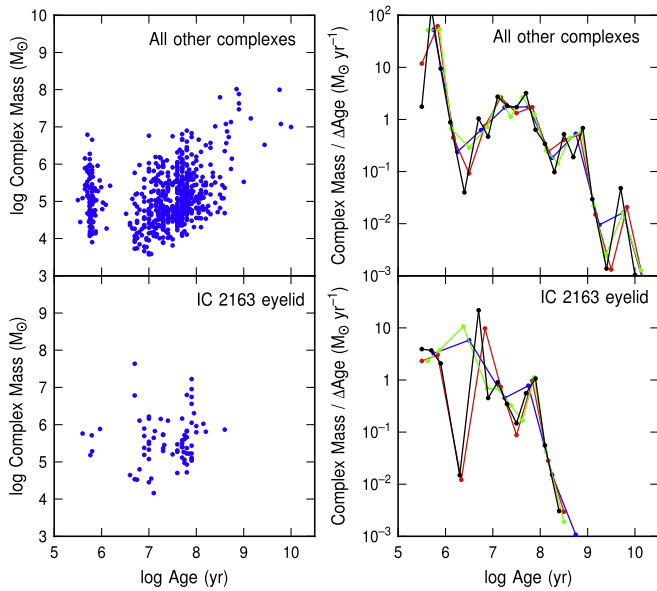


Figure 6. (Left) $\log_{10}(M/M_{\odot})$ vs. $\log(\text{Age})$ for all star complexes outside the eyelids of IC 2163 and in NGC 2207 (top) and inside the eyelids of IC 2163 (bottom). The models are not accurate for ages below 3×10^6 year, so the gap between $\log(\text{Age}) = 6$ and 7 is an artifact. (Right) Summed complex mass per unit $\log(\text{Age})$ interval vs. $\log(\text{Age})$ for all star complexes except the eyelid regions (top) and only the eyelid regions (bottom). Different curves use different bins of $\log(\text{Age})$, which is noted in the text.

the number of complexes in logarithmic age intervals of various lengths, divided by the age intervals (thereby giving rates), are plotted versus the logarithm of age for the eyelid and non-eyelid regions. The variation among the different curves is a result of occasional gaps in the age distribution. In order to determine the number per unit age interval even when there are no star complexes in a particular interval, we include two or three nearby age intervals until there are some complexes, and then divide that number of complexes by the total included age interval. The statistical errors are relatively small for most of the age intervals if we use the inverse square root of the number of complexes as a measure of this error. However, in the ages where the rate drops below ~ 0.1 , the error is of order unity, corresponding to only a few complexes per age interval, as also seen in the left panels. Thus, we estimate that the falloff in the eyelid complex formation rate at $> 2 \times 10^8$ years is a 4σ result, based on $5.2 \pm 0.9\%$ of all 656 complexes that old in non-eyelid regions and 1 complex that old in the eyelids ($1.3 \pm 1.3\%$ of 77 eyelid complexes). To make the eyelid and non-eyelid rate equal, we would need 3 more star complexes in the eyelids with ages larger than 2×10^8 years.

The relatively small number of eyelid complexes older than $\sim 2 \times 10^8$ years is interesting because our models (Struck et al. 2005) suggest that perigalacticon occurred $\sim 2.4 \times 10^8$ years ago. This then is compatible with the encounter having destroyed the older eyelid complexes.

2.6. Correlations between CO Clouds and Star-forming Regions

The positions of the star complexes and clouds were cross-correlated to search for star-forming regions within 300 and 500 pc of the CO clouds. Figure 7 shows star-forming regions as blue dots and CO clouds as red crosses. Lines in the lower left have lengths of 300, 500, and 1200 pc. Black open circles

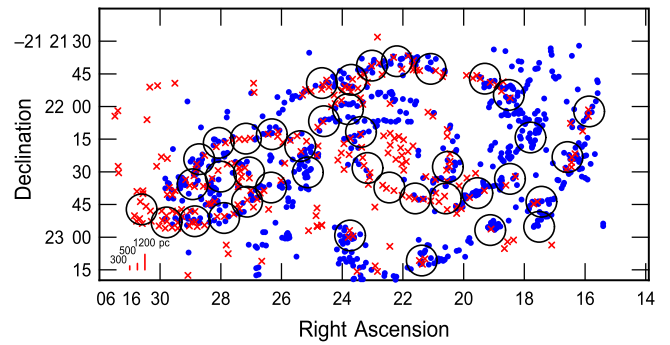


Figure 7. Comparison of CO and star complexes: red crosses represent CO clouds from Figure 2, blue dots are star complexes, and black circles are the 2400 pc diameter SF apertures with prominent $24 \mu\text{m}$ emission and/or $\text{H}\alpha$ emission. The lines in the lower left show the scale for 300, 500, and 1200 pc radii used in the text to determine which star complexes are near CO clouds.

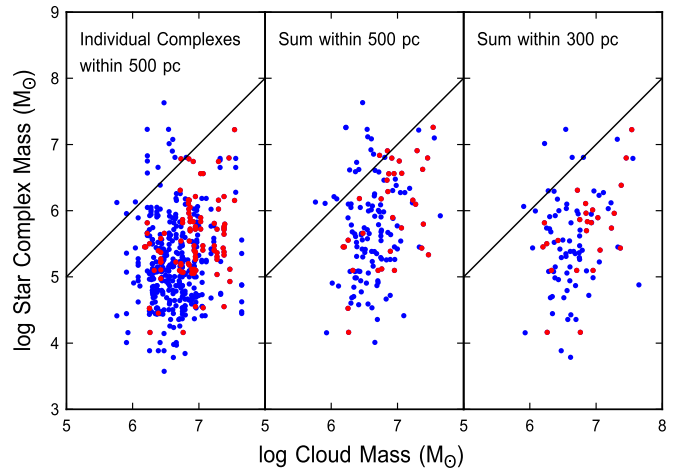


Figure 8. Masses or summed masses of star complexes compared with nearby CO cloud masses. Red dots are for star complexes in the eyelids, and blue dots are for other complexes. (Left) Individual complex masses for all complexes within 500 pc of a CO cloud vs. cloud mass. (middle) Sum of the masses of complexes within 500 pc of a CO cloud vs. cloud mass. (right) Sum of complexes within 300 pc of a CO cloud. The lines represent a fiducial power-law slope of unity with a one-to-one correspondence.

have 2400 pc diameters and are used below to study the large-scale summed emission.

The cross-correlations are used to estimate the average star complex masses that are associated with their adjacent cloud masses. Figure 8 shows a log-log plot of the star complex masses versus the cloud masses. On the left are the CO cloud masses on the abscissa and the individual star complex masses within 500 pc on the ordinate. The red points correspond to regions in the IC 2163 eyelids. The average value of the difference between the log of the complex mass and the log of the cloud mass is -1.41 ± 0.70 , which corresponds to an average ratio of complex mass to cloud mass equal to $\sim 3.9\%$. For the eyelid regions, it is about the same, 4.3%. In the middle panel are the sums of the masses of star-forming regions within 500 pc of a particular CO cloud versus that cloud mass; in the right panel are the sums of the masses of star-forming regions within 300 pc of a CO cloud versus that cloud mass. Red points again represent the eyelids. The lines are fiducial markers showing equality between the complex and cloud masses. The average differences between the log of the summed complex masses and the log of the cloud mass, within these two

distances, are -0.91 ± 0.74 and -1.13 ± 0.69 , respectively; error bars are deviations around the mean. These correspond to ratios of summed star complex mass to CO cloud mass of $\sim 12\%$ and $\sim 7.4\%$ for the two neighborhoods. For the eyelid regions, the ratios of complex/cloud mass are the same within the errors, 12% and 7.0%.

These mass ratios are not the same as star formation efficiencies in any one cloud because we do not know which complex formed in which cloud and because some of the complexes are fairly old, ~ 100 Myr. If we limit the complex age to be less than 30 Myr and the distance to a cloud to be less than 300 pc, then the ratio of the summed complex mass to the cloud mass is 4.4% (4.9% for IC 2163 complexes). These smaller numbers are more typical for star complexes. The higher efficiencies for larger regions may be explained if clouds are younger than the complexes, which span a range of ages, and the complexes build up over time in a sequence of different clouds. It is also possible that the molecular gas was driven out of the regions in which the star complexes formed, or that star complex formation occurred in denser molecular clouds of smaller mass.

Another way to examine the relationship between star-forming regions and CO clouds is with fixed sizes centered on the large-scale star-forming regions. In Paper I we defined regions enclosing prominent $24 \mu\text{m}$ and/or $\text{H}\alpha$ emission, and measured the H I and H_2 masses and star formation rates at these positions. A 2400 pc diameter was chosen to match the resolution of our H I data. Here we determine relative star complex masses on these scales by summing the complex masses and the CO cloud masses within these regions, which we refer to as the ‘‘SF apertures.’’ These apertures are shown by large circles in Figure 7.

Most of the SF apertures contain both CO clouds and star complexes. There are four exceptions: SF apertures A1, A16, A26, and A39 (see Figure 1 in Paper I for labels). A1 (on the eastern tidal arm of IC 2163) contains CO clouds and diffuse star formation but no star complexes, and A26 (on the inner southern arm of NGC 2207 contains CO clouds, $8 \mu\text{m}$, $24 \mu\text{m}$, and diffuse $\text{H}\alpha$ emission, but no star complexes. A16 (between the two galaxies) and A39 (on the western outer arm of NGC 2207) contain star complexes but no CO clouds. The remaining SF apertures contain several CO clouds and star-forming complexes.

Comparisons of CO clouds and star-forming complexes within the SF apertures are shown in Figure 9. The left panel shows each star complex mass versus the total star formation rate in the 2400 pc diameter aperture. The masses of the largest star complexes increase with the star formation rate. The line corresponds to the stellar mass that would result from the SFR on the abscissa in 10^7 years. Most complex masses are less than that, indicating that star formation inside the regions is divided among several complexes that add together to give the total rate. Some of the star formation in each SF aperture has probably taken place outside the identified complexes too. Some complex masses greatly exceed the expected value after 10^7 years, suggesting a longer duration for the accumulation of young stars.

The middle panel shows the sum of the complex masses within the 2400 pc diameter aperture versus the star formation rate. The lines represent the mass that would be made by star formation in 10^7 and 10^8 years. This is a reasonable bracket to the summed complex mass in each 2400 pc region, suggesting

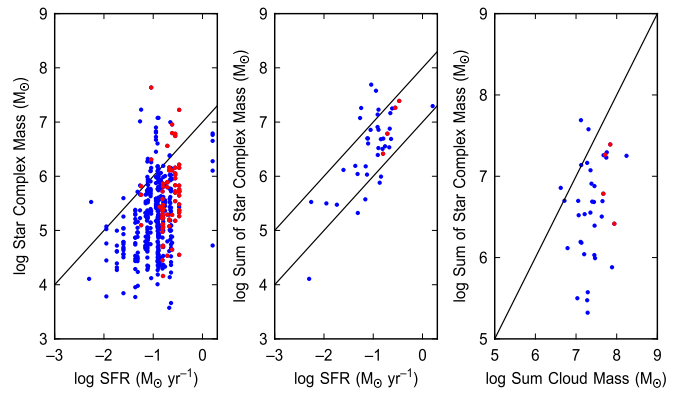


Figure 9. Several properties are shown for optical star complexes and CO clouds within the 2400 pc diameter apertures, as described in Paper I. In all panels, blue dots represent star complexes outside of the eyelids, and red dots represent star complexes in the eyelids of IC 2163. The left panel shows star complexes mass vs. the SFR. The middle panel shows the sum of the complex masses vs. the SFR. The right panel is the sum of the complex masses vs. the sum of the cloud masses within each SF aperture from Paper I, and is equivalent to Figure 8 on larger scales. The lines have unit slope.

a duration of star formation in about this range for the SF apertures.

The right panel of Figure 9 is the sum of the star complex masses versus the sum of the cloud masses within each SF aperture, with the line showing a fiducial slope of unity. This plot is equivalent to Figure 8, but now on a scale of 2400 pc diameter. The average difference between the logarithm of the summed complex mass and the log of the summed cloud mass is -0.78 ± 0.62 , which corresponds to a ratio of star complex mass to CO cloud mass equal to 17%. With only star complexes less than 30 Myr, the mass fraction is 3.9%.

These results for the ratios of young stellar mass to CO cloud mass in various regions around the clouds suggest efficiencies of star formation over 30 Myr periods that are between 3% and 5%. This is normal for OB associations in nearby galaxies (Molinari et al. 2014). The ratios of stellar to molecular masses are larger when we consider all of the stellar complexes near each molecular cloud, suggesting that several generations of OB associations may form before the clouds are destroyed.

2.7. Extinction

Figure 10 shows the average V -band extinction in magnitudes for all of the star complexes within a given SF aperture as measured from the photometric fits versus the sum of the average LOS atomic and molecular column densities for the CO clouds in the aperture. The red dots represent the star complexes in the eyelids, while the blue dots are for complexes not in the eyelids. The line shows the conversion between column density and extinction if assuming one magnitude of extinction at the V -band corresponds to a $1.87 \times 10^{21} \text{ cm}^{-2}$ column density of hydrogen (Bohlin et al. 1978; Draine 2003). The $14''$ diameter apertures used to measure the LOS column densities average out local variations that could be present in the immediate vicinity of the star complexes. On average, the extinction deduced from the neutral hydrogen column densities is about twice the photometrically determined value of A_V of the star complexes. This is consistent with having the star complexes in the midplane and the gas distributed symmetrically about the midplane. The high point of extinction to the upper left of the curve is the central region of IC 2163.

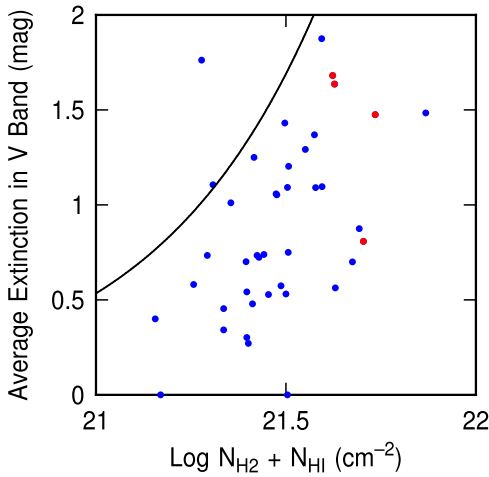


Figure 10. The average extinction in the V -band for the star complexes within a given SF aperture is plotted vs. the log of the average atomic + molecular column density for the clouds within the aperture. The line shows the conversion between column density and extinction based on $N(\text{H}) = 5.8 \times 10^{21} E_{B-V}$ (Bohlin et al. 1978) and the ratio of total to selective extinction $R_V = 3.1$ (Draine 2003).

3. Other High Molecular Column Density Regions

3.1. Star Complexes in Feature i

Feature i is an energetic mini-starburst region in the northwestern tip of NGC 2207; its $\text{H}\alpha$, 8, 24, 70 μm , and radio continuum emission are stronger than anywhere else in the two galaxies, as noted in Elmegreen et al. (2000) and Kaufman et al. (2012). Figure 11 highlights Feature i . The left image is the color composite from F439W in blue, F555W in green, and F814W in red, and the right image is the HST color composite with the CO contours overlaid in green. Note the biconical C-shaped structure of the CO cloud centered on Feature i . Figure 12 shows radio continuum (left) and 8 μm (right) contours on CO intensity maps. The 6 cm and 8 μm emission both peak at the peak CO emission.

Feature i contains $8 \times 10^7 M_\odot$ of molecular gas in the whole triangle outlined by stars (as measured with a $14''$ diameter aperture in Paper I) and $5.9 \times 10^7 M_\odot$ in the C-shaped structure. The southwestern lobe of the C-shaped structure coincides with the optically opaque conically shaped dust cloud (noted in our previous papers) which, in CO, extends $3''.5$ with its axis at position angle P.A. $\sim 220^\circ$ from the central star complex. The other lobe of the C-shaped structure is along the spiral arm.

The central star complex, located at the peak CO column density, has an SED-fitted log mass in M_\odot of 6.31 ± 0.09 and a log age of 5.8 ± 0.4 (0.63 Myr). SExtractor found 13 other star-forming regions within the bright triangle shape in Figure 11, ranging in diameter from 60 pc (12 pixel area) to 100 pc (42 pixel area). The average log mass of these 13 regions is 5.2 ± 0.4 (in M_\odot) and the average log age is 6.9 ± 0.8 (7.9 Myr). Smith et al. (2014) derived an age of 5.7 Myr for a $10''$ diameter aperture around Feature i from the $\text{H}\alpha$ equivalent width. The ratio of the central star complex mass to the CO mass in the C-shaped contour structure of Figure 11 is 3.5%.

Paper I notes that Feature i (measured with a $14''$ diameter aperture) has an SFR of $1.6 M_\odot \text{ yr}^{-1}$, which is very high compared with its gas content, and the gas is HI-dominated in the $14''$

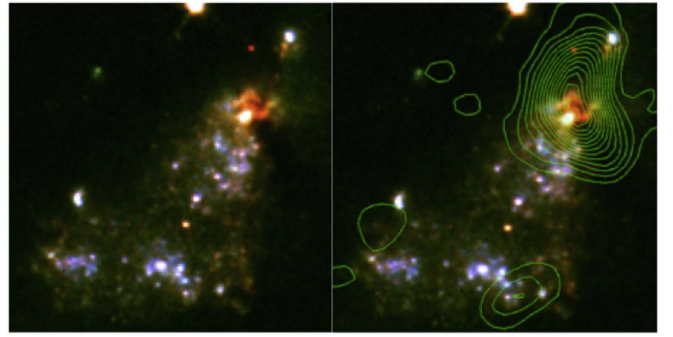


Figure 11. (Left) Feature i in the northwest arm of NGC 2207, shown in HST WFPC2 F439W, F555W, F814W filters. (Right) CO contours in green overlaid on the HST color image. Contour flux values are in linear steps of 66 (Jy beam^{-1}) (m s^{-1}), or $5.8 M_\odot \text{ pc}^{-2}$.

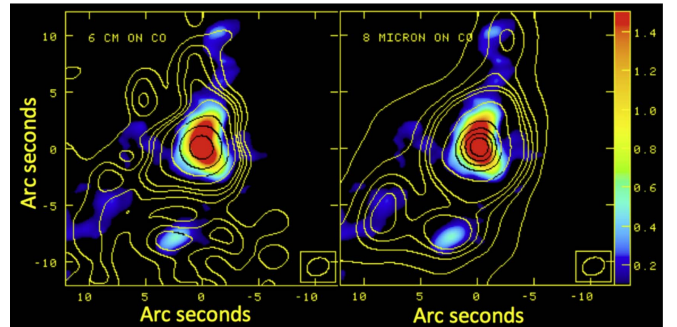


Figure 12. Feature i showing (Left) $\lambda 6$ cm radio continuum contours on CO color, with contour levels of 4, 6, 8, 10, 16, 32, 64, $128 \times$ the rms noise of $0.016 \text{ mJy beam}^{-1}$ (equivalent to $T_b = 0.13 \text{ K}$); and (right) 8 μm contours on CO color, with contour levels of 2, 4, 6, 8, 10, 20, 40, 60, 80, 100 MJy sr^{-1} . The color wedge is in units of $(\text{Jy beam}^{-1})(\text{km s}^{-1})$, where $1 (\text{Jy beam}^{-1})(\text{km s}^{-1})$ corresponds to $88.6 M_\odot \text{ pc}^{-2}$.

aperture. The total neutral hydrogen mass in this aperture is $1.9 \times 10^8 M_\odot$. Thus, for star complexes with ages less than 30 Myr in Feature i , the ratio of the summed star complex mass to total neutral hydrogen mass is 1%.

3.2. NGC 2207 Nuclear Region

NGC 2207 has bright CO in the nuclear region, as shown in Figure 13. The left image shows HST WFPC2 F439W in blue, F555 in green, and F814W in red in a color composite. The central region of NGC 2207 has complex dust lanes with a power-law power spectrum, presumably resulting from turbulence (Elmegreen et al. 1998; Montenegro et al. 1999). The right figure shows CO intensity in grayscale. The red circle is a fiducial reference for both images, which are on the same scale.

There is a double-CO lobe slightly offset from the center of NGC 2207; the northern lobe coincides with optical dust lanes but does not show up at other wavelengths. South of the double lobe is another CO cloud that coincides with optical dust features. The ratio of the northern to southern lobe peak intensity is 0.71. The approximate size of each CO lobe is $4'' \times 3''$, corresponding to $680 \times 510 \text{ pc}$.

A CO ring encircles the central region of NGC 2207, offset slightly north of center, which also shows up in the combined images of both galaxies in Figure 1. The CO ring does not have a counterpart in other wavelengths. Figure 14 shows an enlargement of the central region, with 6 cm contours in CO

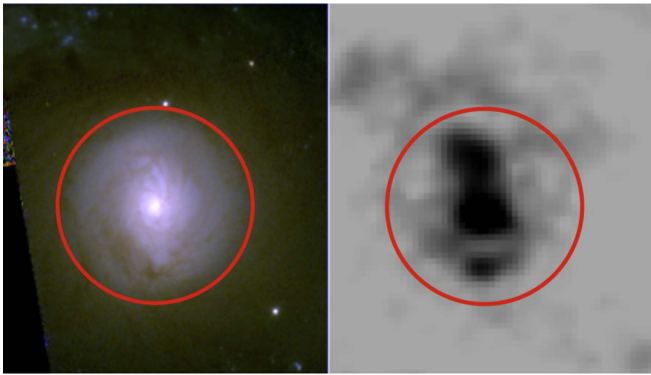


Figure 13. (Left) Nuclear region of NGC 2207 shown in *HST* WFPC2 F439W, F555W, F814W filters; (right) CO on the same scale as the optical color image. The red circle is a fiducial marker for the two images.

grayscale emission on the left (with the CO image convolved to the $2''.5$ resolution of the radio image), and non-stellar $8\ \mu\text{m}$ contours on CO intensity grayscale emission on the right. The non-stellar $8\ \mu\text{m}$ component was calculated from IRAC 4-0.232 IRAC 1 using the recipe of Helou et al. (2004) (This overestimates the correction since IRAC 1 contains some PAH bands.) The non-stellar $8\ \mu\text{m}$ here is presumably from excitation by the general radiation field in the nucleus, not star-forming regions.

The CO emission is elongated, possibly a mini-bar, whereas the radio continuum emission shows a slight elongation perpendicular to the CO mini-bar and along the direction of the kinematic major axis. It is possible that the CO ring is a resonance related to the mini-bar.

The locations of maximum brightness in the N2207 nucleus in 6 cm radio continuum and $8\ \mu\text{m}$ coincide, within the uncertainties, with the *Chandra* position listed by Mineo et al. (2014) of a low-luminosity AGN X-ray source in N2207, which has a nonsymmetric shape of the central AGN in X-rays. The radio continuum is probably from the AGN. The molecular gas is probably dissociated at the location of the AGN, which helps produce the double-lobed appearance. The location of peak CO emission is $1''$ south of the AGN.

4. Conclusions

Over 200 large-scale molecular emission regions with masses down to $\sim 10^6 M_\odot$ have been identified in the interacting galaxies IC 2163 and NGC 2207. These clouds contain about half of the total CO mass in the two galaxies detected by the interferometer. The eyelid regions of IC 2163 contain the clouds with the highest average mass; all have $\log_{10}(M/M_\odot)$ greater than 6.6, and an average of 7.2. The ages of the star complexes in the eyelids are younger than $\sim 2 \times 10^8$ year, similar to the time of interaction of the two galaxies, whereas some star complexes in NGC 2207 are older. This suggests that the processes that formed the eyelids destroyed the complexes there.

The mass distribution functions of the CO clouds follow a power-law distribution, as do the star complexes identified down to masses of about $10^5 M_\odot$ both in the eyelid regions and elsewhere in the galaxies. The clouds in NGC 2207 have a steeper mass distribution function than those in the IC 2163 eyelids or in the inner parts of the Milky Way, but that function is comparable to those in the outer parts of the Milky Way and

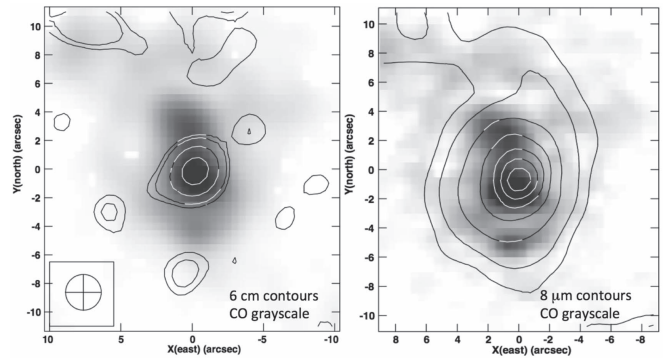


Figure 14. (Left) Overlay of 6 cm radio continuum contours on grayscale CO emission for the nuclear region of NGC 2207; the contours are at 3, 4, 8, 16, 32, 64 times the rms noise of $0.016\ \text{mJy beam}^{-1}$. (Right) Overlay of non-stellar $8\ \mu\text{m}$ contours on CO grayscale intensity. The contour levels are at 3, 4, 6, 8, 10, 12, 14 MJy sr^{-1} .

M33. To explain these variations, we considered the possibility that the CO cloud mass function is steeper than the total cloud mass function in regions with low molecular fraction as a result of a decrease in the CO mass fraction with increasing total cloud mass.

The ratio of the summed star complex mass within 500 pc of a molecular cloud to the cloud mass is $\sim 12\%$ in these galaxies; within 300 pc, it is $\sim 7\%$. For 40 star-forming regions 2.4 kpc in diameter, the ratio of the summed star complex mass to the summed H_2 mass is $\sim 17\%$. These ratios are higher than the efficiencies of star formation in any one cloud. For complexes younger than 30 Myr and within 300 pc of a cloud, the ratio of stellar to gas mass is $\sim 4\%$, and for complexes younger than 30 Myr in the 2.4 kpc regions, it is also $\sim 4\%$. For the mini-starburst Feature *i*, the ratio of the mass of the central star complex to the total CO mass around it is 3.5%.

The average star complex extinctions scale with increasing gas column density, suggesting that the CO gas is in the midplane and not preferentially on one side from the interaction of the two galaxies.

The nuclear region of NGC 2207 contains a double-lobed CO cloud, possibly a mini-bar. It is surrounded by a molecular ring, which could be the result of a resonance associated with the mini-bar. It contains the most massive cloud in the system.

E.B. acknowledges support from the UK Science and Technology Facilities Council [grant number ST/M001008/1]. This paper used the following ALMA data: ADS/JAO.ALMA#2012.1.00357.S. ALMA is a partnership of ESO (representing its member states), NSF (USA) and NINS (Japan), together with NRC (Canada) and NSC and ASIAA (Taiwan) and KASI (Republic of Korea), in cooperation with the Republic of Chile. The Joint ALMA Observatory is operated by ESO, AUI/NRAO, and NAOJ. The National Radio Astronomy Observatory is a facility of the National Science Foundation operated under cooperative agreement by Associated Universities, Inc. This research used the NASA/IPAC Extragalactic Database (NED), which is operated by the Jet Propulsion Laboratory, California Institute of Technology, under contract with the National Aeronautics and Space Administration. We thank the referee, Dr. Erik Rosolowsky, for helpful comments that improved the clarity of the paper.

References

- Bertin, E., & Arnouts, S. 1996, *A&AS*, **117**, 393
- Block, D. L., Puerari, I., Elmegreen, B. G., & Bournaud, F. 2010, *ApJ*, **718**, 1
- Bohlin, R., Savage, B., & Drake, J. 1978, *ApJ*, **224**, 132
- Bruzual, G., & Charlot, S. 2003, *MNRAS*, **344**, 1000
- Calzetti, D., Armus, L., Bohlin, R. C., et al. 2000, *ApJ*, **533**, 682
- Colombo, D., Hughes, A., Schinnerer, E., et al. 2014, *ApJ*, **784**, 3
- Combes, F., Boquien, M., Kramer, C., et al. 2012, *A&A*, **539**, 67
- Condon, J. J. 1992, *ARA&A*, **30**, 575
- Dame, T. M., Hartmann, D., & Thaddeus, P. 2001, *ApJ*, **655**, 863
- Draine, B. T. 2003, *ARA&A*, **41**, 241
- Efremov, Y. N. 1995, *AJ*, **110**, 2757
- Elmegreen, B. G., Elmegreen, D. M., Brinks, E., et al. 1998, *ApJL*, **503**, L119
- Elmegreen, B. G., & Hunter, D. A. 2010, *ApJ*, **712**, 604
- Elmegreen, B. G., & Hunter, D. A. 2015, *ApJ*, **805**, 145
- Elmegreen, B. G., Kaufman, M., Bournaud, F., et al. 2016, *ApJ*, **823**, 26 (Paper I)
- Elmegreen, B. G., Kaufman, M., Struck, C., et al. 2000, *AJ*, **120**, 630
- Elmegreen, B. G., Kim, S., & Staveley-Smith, L. 2001, *ApJ*, **548**, 74
- Elmegreen, B. G., Sundin, M., Kaufman, M., Brinks, E., & Elmegreen, D. M. 1995b, *ApJ*, **453**, 139
- Elmegreen, D. M., Elmegreen, B. G., Kaufman, M., et al. 2006, *ApJ*, **642**, 158
- Elmegreen, D. M., Elmegreen, B. G., Sánchez Almeida, J., et al. 2012, *ApJ*, **750**, 95
- Elmegreen, D. M., Kaufman, M., Brinks, E., Elmegreen, B. G., & Sundin, M. 1995a, *ApJ*, **453**, 100
- Elmegreen, D. M., Kaufman, M., Elmegreen, B. G., et al. 2001, *AJ*, **121**, 182
- Golla, G., Allen, M., & Kronberg, P. 1996, *ApJ*, **473**, 244
- Gratier, P., Braine, J., Rodríguez-Fernández, N. J., et al. 2012, *A&A*, **542**, A108
- Helou, G., Roussel, H., Appleton, P., et al. 2004, *ApJS*, **154**, 253
- Hunter, D. A., Elmegreen, B. G., Dupuy, T. J., & Mortonson, M. 2003, *AJ*, **126**, 1836
- Kaufman, M., Elmegreen, B. G., Struck, C., et al. 2016, *ApJ*, **831**, 161
- Kaufman, M., Grupe, D., Elmegreen, B. G., et al. 2012, *AJ*, **144**, 156
- Kennicutt, R. C., & Evans, N. J. 2012, *ARA&A*, **50**, 531
- Kennicutt, R. C., Jr., Calzetti, D., Walter, F., et al. 2007, *ApJ*, **671**, 333
- Koda, J., Scoville, N., Sawada, T., La Vigne, M., Vogel, S., et al. 2009, *ApJ*, **700**, L132
- Larson, R. B. 1981, *MNRAS*, **194**, 809
- Leitherer, C., Li, I.-H., Calzetti, D., & Heckman, T. M. 2002, *ApJS*, **140**, 303
- Mineo, S., Rappaport, S., Levine, A., et al. 2014, *ApJ*, **797**, 91
- Mivilhe-Deschênes, M.-A., Murray, N., & Lee, E. J. 2017, *ApJ*, **834**, 57
- Molinari, S., Bally, J., Glover, S., et al. 2014, in *Protostars and Planets VI*, ed. H. Beuther et al. (Tucson, AZ: Univ. Arizona Press), 125
- Montenegro, L., Yuan, C., & Elmegreen, B. G. 1999, *ApJ*, **520**, 592
- Rosolowsky, E. 2005, *PASP*, **117**, 1403
- Rosolowsky, E., Keto, E., Matsushita, S., & Willner, S. P. 2007, *ApJ*, **661**, 830
- Rupke, D., Kewley, L., & Chien, L.-H. 2010, *ApJ*, **723**, 1255
- Sánchez, N., Alfaro, E. J., & Pérez, E. 2005, *ApJ*, **625**, 849
- Shadmehri, M., & Elmegreen, B. G. 2011, *MNRAS*, **410**, 788
- Smith, B., Soria, R., Struck, C., et al. 2014, *AJ*, **147**, 60
- Stanimirovic, S., Staveley-Smith, L., Dickey, J. M., Sault, R. J., & Snowden, S. L. 1999, *MNRAS*, **302**, 417
- Stanimirovic, S., Staveley-Smith, L., van der Hulst, J. M., et al. 2000, *MNRAS*, **315**, 791
- Struck, C., Kaufman, M., Brinks, E., et al. 2005, *MNRAS*, **364**, 69
- Vila, M., Pedlar, A., Davies, R., Hummel, E., & Axon, D. 1990, *MNRAS*, **242**, 379
- Wei, L., Keto, E., & Ho, L. 2012, *ApJ*, **750**, 136
- Wild, W., Harris, A., Eckart, A., et al. 1992, *A&A*, **265**, 447
- Zhang, H.-X., Hunter, D. A., & Elmegreen, B. G. 2012, *ApJ*, **754**, 29